Title

Protagonists and spectators during photocatalytic solar water splitting with $SrTaO_xN_y$ oxynitride.

Authors

Craig Lawley,[a,b] Zahra Pourmand Tehrani,[a,b] Adam H. Clark,[a] Olga V. Safonova,[a] Max Döbeli,[c] Vladimir N. Strocov,[a] Thomas J. Schmidt,[a,d] Thomas Lippert,[a,b,e] Maarten Nachtegaal,*[a] Daniele Pergolesi*[a]

Author Affiliations

[a]Paul Scherrer Institute, CH-5232 Villigen PSI.

[b]ETH Zürich, Laboratory of Inorganic Chemistry, CH-8093 Zurich.

[c]ETH Zürich, Laboratory of Ion Beam Physics, CH-8093 Zurich.

[d]ETH Zürich, Laboratory of Physical Chemistry, CH-8093 Zurich.

[e]International Institute for Carbon-Neutral Energy Research (I2CNER), Kyushu University, 744 Motooka 819-0395 Fukuoka, Japan

Correspondence to: Dr. D. Pergolesi (E-mail: daniele.pergolesi@psi.ch), Dr. M. Nachtegaal (E-mail: maarten.nachtegaal@psi.ch).

Abstract

Oxynitrides have been shown to be promising visible light water splitting photocatalysts, but rapidly degrade under operating conditions. With a custom designed photoelectrochemical cell, we perform operando grazing incidence X-ray absorption spectroscopy measurements on the oxynitride semiconductor SrTaOxNy during photocatalytic solar water splitting. We show that the nature of the A-site (Sr) and its evolution during operation, have large impacts on the overall stability and catalytic acitivity of the material, leading to an enriched BO2 (Ta(OH)/TaO(OH)) like surface. However, this usually beneficial effect with respect to increased surface hydrophilicity has complications for the efficiency of the photocatalytic process, as the OH and O(OH) intermediates formed are in competition between O2 generation and NOx species formation in the initial stages of operation. Operando characterisation of the evolution of the electronic structure of the photocatalyst proves to be an invaluable tool for the rational design and discovery of new and better performing materials.

Supplementary Figures

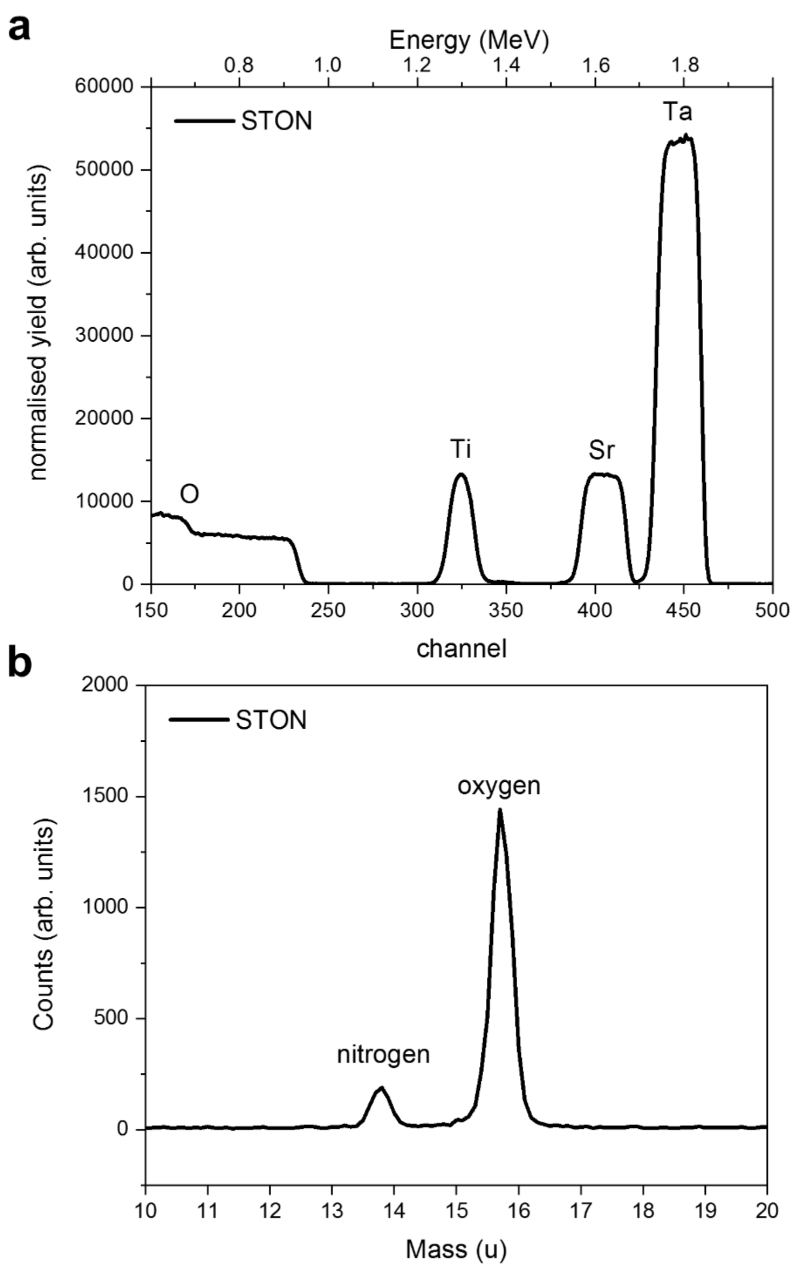

Supplementary Figure 1. Ion beam analysis of STON thin films. (a) Rutherford backscattering (RBS) spectrum, (b) elastic recoil detection analysis (ERDA) spectrum. The cation ratios were determined by RBS and the O:N ratio by ERDA.

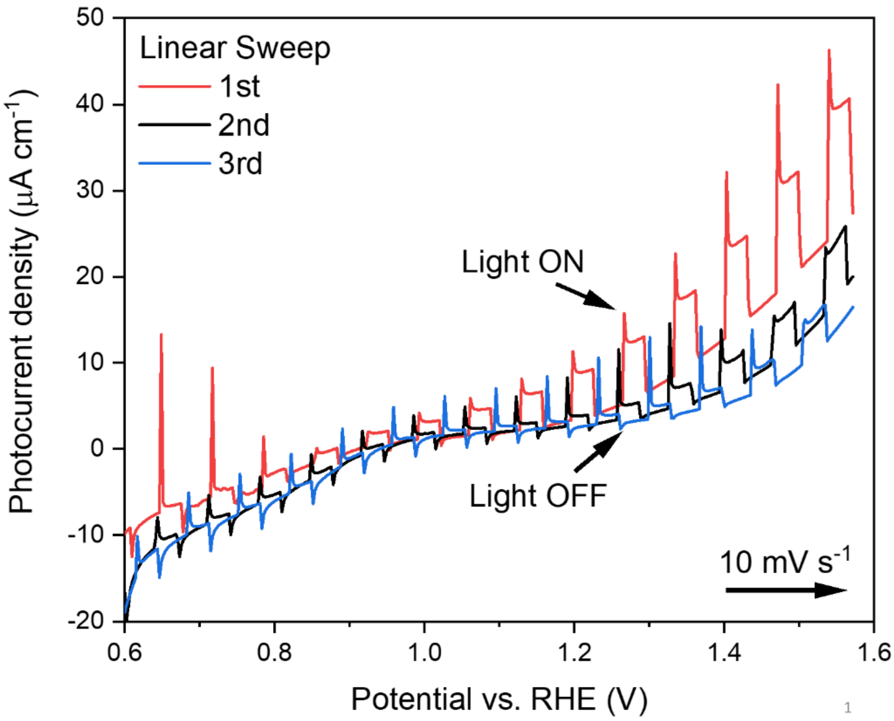

Supplementary Figure 2. Photoelectrochemical characterisation.

Photocurrent densities for STON for the first three potentiodynamic measurements, showing initial degradation.

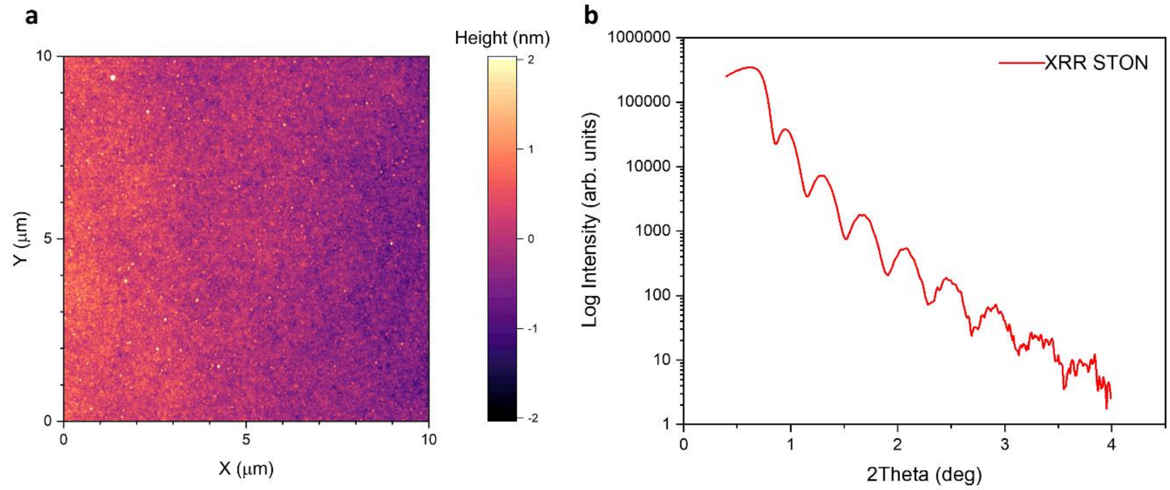

Supplementary Figure 3. Surface roughness characterisation. (a) Atomic force microscopy characterization of the STON film surface. (b) X-ray reflectometry measurement of a STON film grown on MgO.

The RMS roughness across the entire 10x10 µm scan area was 409.6 pm. Scan details are as follows: 10 µm x/y dimensions, 512 lines, 3 s per line. Tapping mode in air with Nanosensors PPP-NCLR cantilevers – ca. 190 kHz resonance frequency, spring constant k is ca. 48 N/m. In addition, we also include an example XRR measurement for the STON films that we grow and use as a method to calibrate the deposition rate for each material. The multiple oscillations and intensity, clearly signify the thickness homogeneity and the lack of pronounced roughness

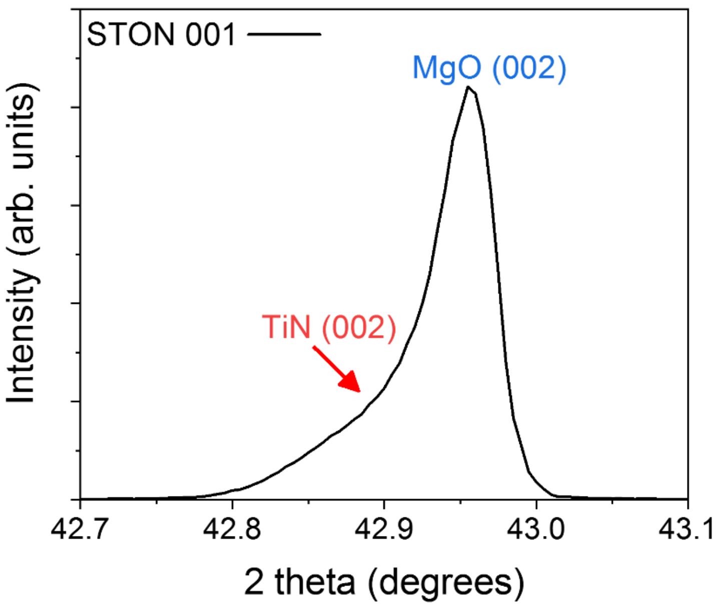

Supplementary Figure 4. XRD. Zoomed region around the MgO substrate reflex for data shown in Figure 2.

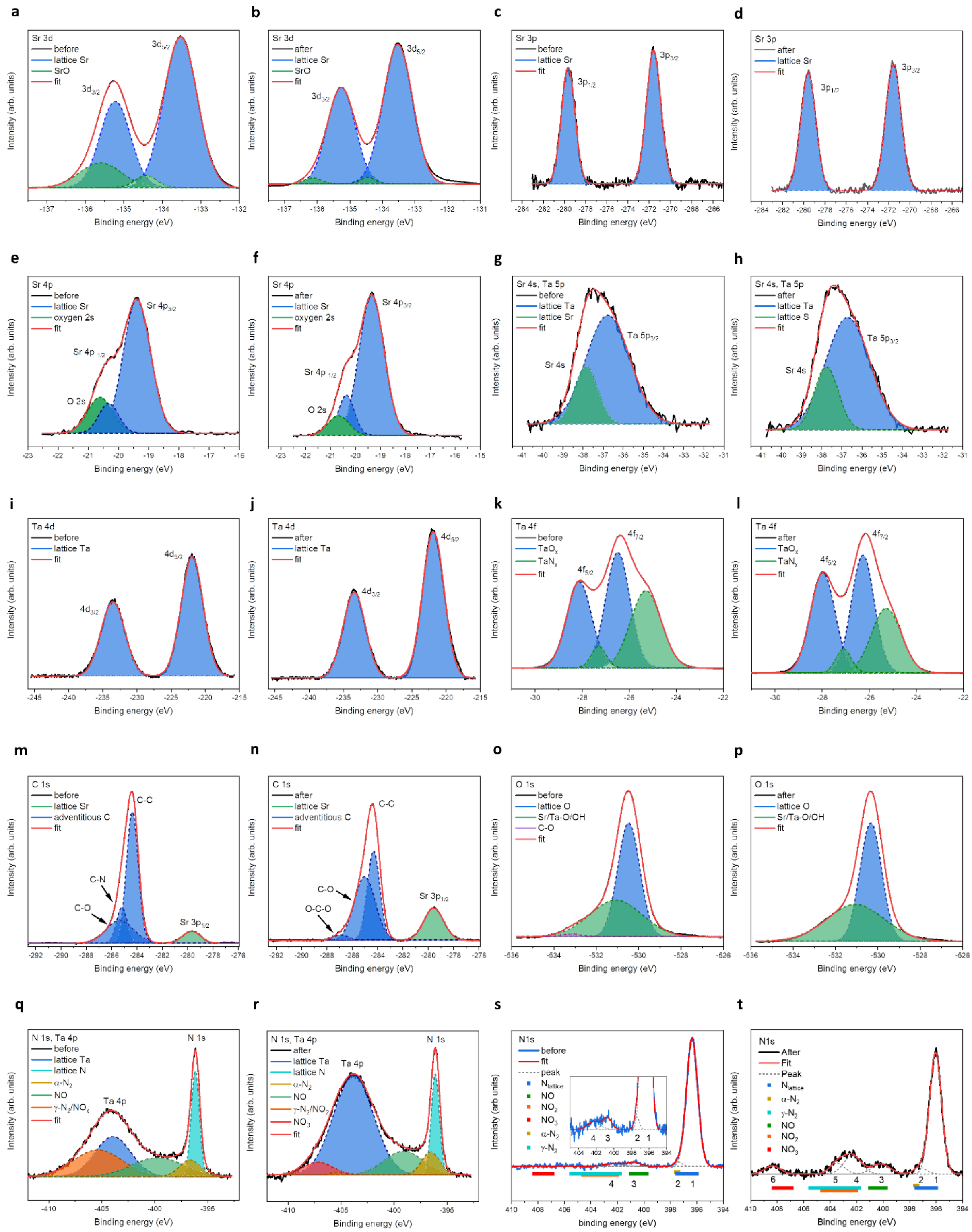

Supplementary Figure 5. XPS peak fitting. (a-r) STON before and after PEC, (s-t) LTON N1s before and after PEC, respectively. Reference values for binding energies given in supplementary tables.

a

b

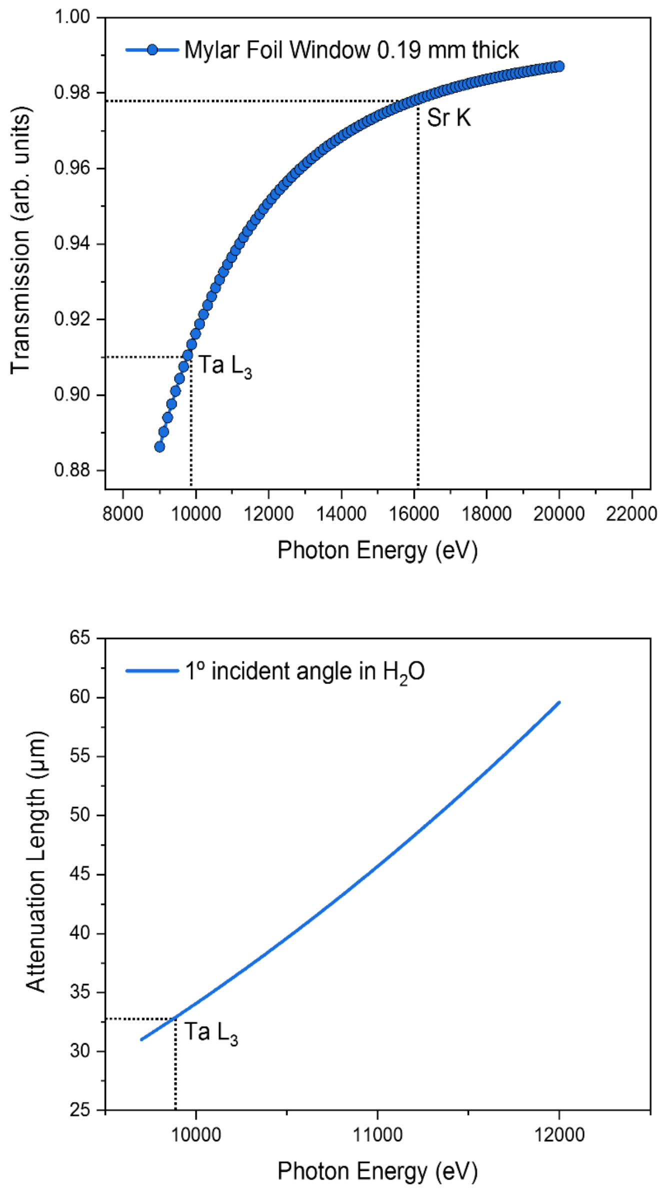

Supplementary Figure 6. (a) Transmission of X-rays through optically clear Mylar used as a window material for X-rays and visible light, (b) attenuation length of X-rays in pure H2O at an incident angle of 1°. Ta L3 edge (9881 eV) has been labelled (Sr K edge at 16105 eV is not shown). Values taken from[1].

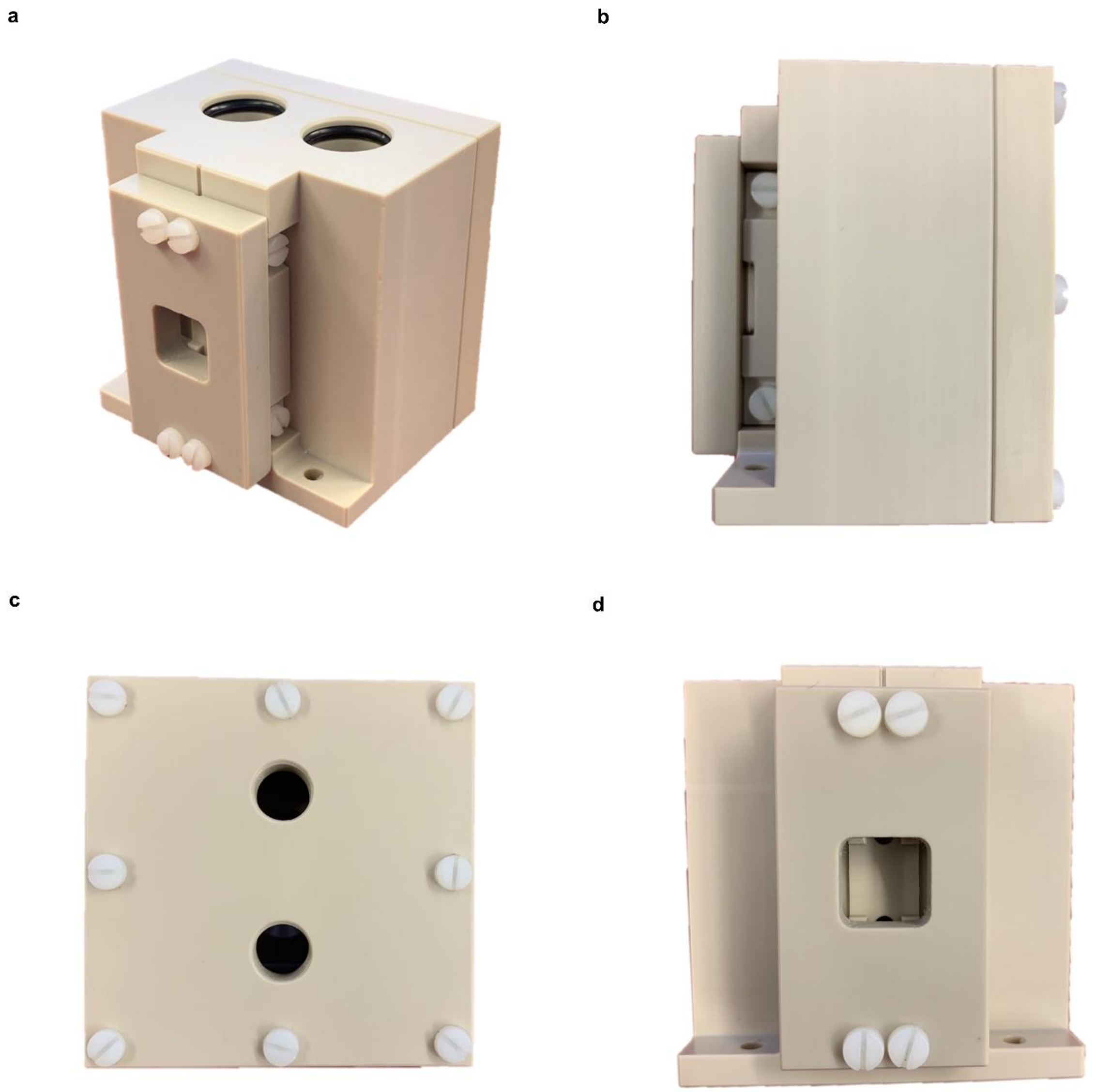

Supplementary Figure 7. *Operando* reactor cell. (a) Trimetric view, (b) side view, (c) back side with fittings for a peristaltic pump or for sealing, (d) front view. The cell was designed and fabricated at the Paul Scherrer Institute as part of this work.

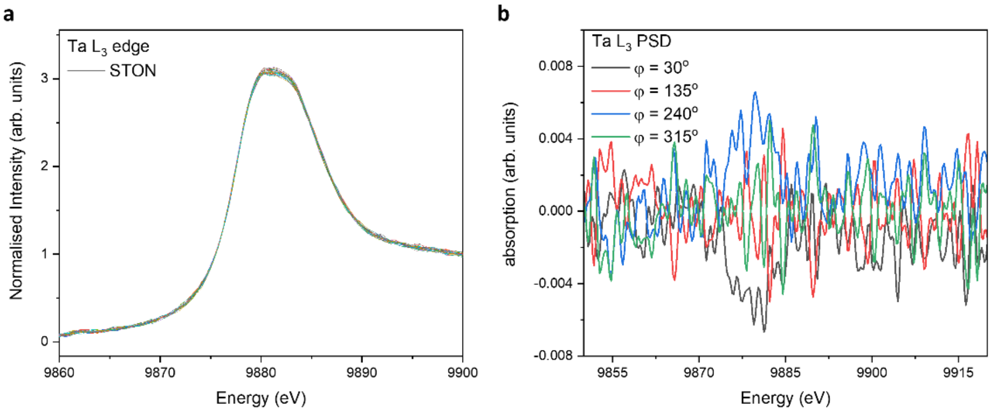

Supplementary Figure 8. Ta L_3 spectra recorded under illumination and under dark conditions. The Ta PSD signal does not exhibit any changes larger than the noise of the experiments. This does not suggest that Ta is not active, rather that the changes in electron density and the kinetics of the OER are much faster than those for Sr due to the fact that Ta is a transition metal and Sr, an alkaline earth element.

Supplementary Tables

Supplementary Table 1. Ion Beam Analysis.

Composition	Sr:Ta	O:N
$Sr_{0.94}Ta_{1.06}O_{2.80}N_{0.31}$	0.89 (0.02)	9.03(0.07)

Supplementary Table 2. Literature sourced XPS data for Ta $4p_{3/2}$.

Component	Energy (eV)	Reference
TaN_x	400.8	2
	402	3
	403	4
TaO_xN_y	403.1	5
	403.5	6
	403.9	5
	404	7
	404.5	8

Supplementary Table 3. Literature sourced XPS data for N1s.

Component	Energy (eV)	Reference
$N_{(L)}$	396-397.5	2, 8-21
α-$N_{2(c)}$	397.5	11
$NO_{(i)}$	399.8	15
$NO_{(c)}$	400	22
	400.4	14
	400.9	23
	401	13
γ-$N_{2(c)}$	401.8	10
	403	15
	405	11
	405.5	24
$NO2_{(c)}$	402	13
	403.5	25
	403.6	18
	404.6	26
$NO3_{(c)}$ / -O-NO2	406.9	27
	407	25
	407.2	16
	407.4	18

Where (L), (C) and (i) correspond to lattice, chemisorbed and interstitial respectively.

Supplementary Table 4. Literature sourced XPS data for O1s.

Component	Energy (eV)	Reference
Ta-$O_{(L)}$	528.2-531.4	2, 6-8, 28-33
$OH_{(c)}$	531.3	34
	531.4	10
	531.5	35
	531.6	36, 37
	532.0	33
	532.1	31, 38
	532.4	31, 39
$H2O_{(c)}$	533.0	36
	533.3	34
	533.7	37
	533.9	40
	534.7	41

Supplementary Table 5. Sr 3p Peak Fit Before PECR

Peak	1	2
Centroid (eV)	-279.65322 ± 0.00457	-271.58483 ± 0.00409
FWHM (eV)	1.291 ± 0.0096	1.36436 ± 0.00861
Area	24249.73794 ± 170.28232	29469.15676 ± 176.22869
R-Square	0.99493	

Supplementary Table 6. Sr 3p Peak Fit After PECR

Peak	1	2
Centroid (eV)	-279.57941 ± 0.00317	-271.53526 ± 0.003
FWHM (eV)	1.4441 ± 0.00672	1.47716 ± 0.00637
Area	42598.5652 ± 189.56348	46526.0029 ± 192.31561
R-Square	0.99776	

Supplementary Table 7. Sr 3d Peak Fit Before PECR

Peak	1	2	3	4
Centroid (eV)	--133.52559 ± 0.01414	-134.42294 ± 0.15156	-135.22127 ± 0.04092	-135.60325 ± 5.33923
FWHM (eV)	0.86754 ± 0.02092	0.55329 ± 0.30998	0.79233 ± 0.55571	1.09281 ± 2.65848
Area	220674.28476 ± 6504.05398	11457.0213 ± 2241.51213	115215.53577 ± 54773.7724	6112.76107 ± 5108.96732
R-Square	0.98726			

Supplementary Table 8. Sr 3d Peak Fit After PECR

Peak	1	2	3	4
Centroid (eV)	-133.52371 ± 0.00375	-134.44716 ± 0.07153	-135.25871 ± 0.00981	136.13358 ± 0.15463
FWHM (eV)	0.90477 ± 0.00793	0.4245 ± 0.15984	0.86069 ± 0.04955	0.5591 ± 0.19969
Area	232332.42423 ± 1776.72603	5212.77251 ± 4145.0633	153051.89003 ± 8408.25997	45995.00203 ± 1424.5185
R-Square	0.99609			

Supplementary Table 9. Sr 4p and O 2s Peak Fit Before PECR

Peak	1	2	3
Centroid (eV)	-19.38482 ± 0.01864	-20.3163 ± 0.10708	-20.61054 ± 1.16868
FWHM (eV)	0.9026 ± 0.01591	0.64963 ± 0.43078	0.83051 ± 0.52531
Area	11953.29605 ± 495.33252	1912.54469 ± 1122.8581	2959.82432 ± 1170.0807
R-Square	0.99918		

Supplementary Table 10. Sr 4p and O 2s Peak Fit After PECR

Peak	1	2	3
Centroid (eV)	-19.34974 ± 0.01268	-20.36315 ± 0.04252	-20.68429 ± 1.15995
FWHM (eV)	1.00048 ± 0.013	0.63186 ± 0.18837	0.84706 ± 0.57905
Area	16509.95251 ± 391.78648	2985.39928 ± 654.02432	1944.41958 ± 690.44717
R-Square	0.99918		

Supplementary Table 11. Sr 4s and Ta 5p Peak Fit Before PECR

Peak	1	2
Centroid (eV)	-37.83893 ± 0.01823	-36.75281 ± 0.06538
FWHM (eV)	1.16559 ± 0.07543	2.17036 ± 0.06255
Area	4220.6715 ± 803.01647	14750.36267 ± 922.61298
R-Square	0.99446	

Supplementary Table 12. Sr 4s and Ta 5p Peak Fit After PECR

Peak	1	2
Centroid (eV)	-37.75081 ± 0.01553	-36.69728 ± 0.05493
FWHM (eV)	1.19942 ± 0.06123	2.19563 ± 0.05015
Area	6106.5987 ± 926.47299	19927.18315 ± 1056.30328
R-Square	0.9963	

Supplementary Table 13. Ta 4d Peak Fit Before PECR

Peak	1	2
Centroid (eV)	-233.5189 ± 0.00585	-221.91514 ± 0.0035
FWHM (eV)	3.48002 ± 0.01311	3.2174 ± 0.00777
Area	102869.76637 ± 398.19966	152900.35078 ± 376.43228
R-Square	0.99841	

Supplementary Table 14. Ta 4d Peak Fit After PECR

Peak	1	2
Centroid (eV)	-233.41751 ± 0.00665	-221.85157 ± 0.0038
FWHM (eV)	3.27951 ± 0.01474	3.13172 ± 0.00839
Area	132220.62551 ± 602.56733	215880.03097 ± 583.29846
R-Square	0.998	

Supplementary Table 15. Ta 4f Peak Fit Before PECR

Peak	1	2	3	4
Centroid (eV)	-25.28531 ± 0.01644	-27.2936 ± 0.0139	-26.48192 ± 0.0056	-28.12081 ± 0.00614
FWHM (eV)	1.30442 ± 0.01537	0.63056 ± 0.03194	1.03484 ± 0.02117	1.0662 ± 0.00779
Area	125778.64569 ± 3126.10392	17090.70087 ± 2890.97467	149256.04267 ± 5148.01471	114674.56033 ± 1192.47262
R-Square	0.99987			

Supplementary Table 16. Ta 4f Peak Fit After PECR

Peak	1	2	3	4
Centroid (eV)	-25.26927 ± 0.03279	-27.08503 ± 0.01872	-26.26536 ± 0.00667	-27.9737 ± 0.00524
FWHM (eV)	1.26866 ± 0.02643	0.97409 ± 0.02477	0.66245 ± 0.03494	1.05826 ± 0.00665
Area	132232.36396 ± 7017.27026	185156.91357 ± 10048.03592	25633.93592 ± 4493.3563	171320.72122 ± 1535.28089
R-Square	0.99987			

Supplementary Table 17. C 1s Peak Fit Before PECR

Peak	1	2	3	4
Centroid (eV)	-279.69471 ± 0.00839	-284.3548 ± 0.00767	-285.18928 ± 0.02152	-285.35279 ± 0.0267
FWHM (eV)	1.39118 ± 0.01775	0.93911 ± 0.00887	0.82405 ± 0.0233	2.13579 ± 0.03022
Area	29309.94428 ± 357.69729	214157.2881 ± 4433.23097	51158.70353 ± 4217.75904	84350.46265 ± 2540.20022
R-Square	0.99976			

Supplementary Table 18. C 1s Peak Fit After PECR

Peak	1	2	3	4
Centroid (eV)	-279.57921 ± 0.00335	-284.31246 ± 0.00388	-285.01138 ± 0.02467	-286.92129 ± 0.06273
FWHM (eV)	1.55878 ± 0.00715	0.97561 ± 0.00901	1.64606 ± 0.01545	1.1534 ± 0.08275
Area	50003.16423 ± 221.61098	86330.86346 ± 2788.01509	103841.19401 ± 2414.48879	5983.695 ± 764.23011
R-Square	0.99971			

Supplementary Table 19. O 1s Peak Fit Before PECR

Peak	1	2	3
Centroid (eV)	-530.46148 ± 0.00178	-531.07071 ± 0.0374	-533.18451 ± 0.05187
FWHM (eV)	1.04254 ± 0.00626	2.48263 ± 0.0627	0.9018 ± 0.17859
Area	165610.48771 ± 2829.38261	126647.74654 ± 1471.86872	3398.38014 ± 1501.12366
R-Square	0.99979		

Supplementary Table 20. O 1s Peak Fit After PECR

Peak	1	2
Centroid (eV)	-530.32002 ± 0.00106	-531.04871 ± 0.00807
FWHM (eV)	1.03305 ± 0.00275	2.73542 ± 0.01428
Area	295971.82056 ± 1368.69256	243648.68368 ± 1828.90827
R-Square	0.99983	

Supplementary Table 21. N 1s and Ta 4p Peak Fit Before PECR

Peak	1	2	3	4
Centroid (eV)	-396.15118 ± 0.00378	-396.65639 ± 0.09367	-399.67412 ± 1.88024	-403.92705 ± 0.10212
FWHM (eV)	0.79614 ± 0.00996	1.94654 ± 0.21381	4.87092 ± 1.3796	3.38278 ± 1.1459
Area	21611.22085 ± 568.30918	8370.54043 ± 2479.53865	22418.31898 ± 5377.99719	96803.94916 ± 10607.91758

Peak	5
Centroid (eV)	-405.35034 ± .28803
FWHM (eV)	4.61057 ± 3.03883
Area	31680.48163 ± 15843.03548
R-Square	0.99653

Supplementary Table 22. N 1s and Ta 4p Peak Fit After PECR

Peak	1	2	3	4
Centroid (eV)	-396.0752 ± 0.00465	-396.51934 ± 0.07196	-399.06478 ± 0.30341	-403.80418 ± 0.08599
FWHM (eV)	0.76585 ± 0.01237	1.68271 ± 0.13794	3.65362 ± 0.59233	3.76847 ± 0.31262
Area	19835.05122 ± 748.6462	9909.66385 ± 1928.76987	22418.31898 ± 5377.99719	96803.94916 ± 10607.91758

Peak	5	6
Centroid (eV)	-405.41358 ± 0.21635	-407.1659 ± 0.48547
FWHM (eV)	1.14905 ± 0.65182	2.78483 ± 0.39213
Area	750.00707 ± 1037.78766	9226.66389 ± 6274.80751
R-Square	0.99764	

Supplementary Discussion

Phase Sensitive Detection (PSD)

PSD is a mathematical function, which converts time-resolved XAS data into a set of phase-resolved data post acquisition, enhancing sensitivity of the modulated excitation XAS experiment.

The time-resolved data $I(t)$ are converted into phase-resolved data $I(\varphi^{\mathrm{PSD}})$ with a demodulation phase angle ($0° < \varphi^{\mathrm{PSD}} < 360°$) according to the following equation:

$$I(\varphi^{PSD}) = \frac{2}{T}\int_0^T I(t)\sin(n\omega t + \varphi^{PSD})\, dt$$

Where T is the stimulation period, $\omega(2\pi/T)$ is the angular frequency and $n\omega$ the demodulation frequency.

For n=1 (fundamental frequency) the demodulation frequency is equal to the stimulation frequency. Harmonic frequencies are also obtained (n=2, 3 . . .) and the signal intensity of the PSD varies harmonically as φ^{PSD} varies between 0 and 2π.

The major advantage in using PSD, is that it yields a set of phase-resolved data which contains primarily the signals from the changes due to the external stimulus. Further information on PSD and its applications can be found here.[42-45]

Supplementary References

1. B. L. Henke, E. M. Gullikson and J. C. Davis, *At. Data Nucl. Data Tables*, 1993, **54**, 181-342.
2. P. Lamour, P. Fioux, A. Ponche, M. Nardin, M.-F. Vallat, P. Dugay, J.-P. Brun, N. Moreaud and J.-M. Pinvidic, *Surf. Interface Anal.*, 2008, **40**, 1430-1437.
3. M. Alishahi, F. Mahboubi, S. M. Mousavi Khoie, M. Aparicio, E. Lopez-Elvira, J. Méndez and R. Gago, *RSC Advances*, 2016, **6**, 89061-89072.
4. A. Zaman and E. Meletis, *Coatings*, 2017, **7**.
5. H. Fu, S. Zhang, L. Zhang and Y. Zhu, *Mater. Res. Bull.*, 2008, **43**, 864-872.
6. S. Khan, M. J. Zapata, M. B. Pereira, R. V. Goncalves, L. Strizik, J. Dupont, M. J. Santos and S. R. Teixeira, *Phys. Chem. Chem. Phys.*, 2015, **17**, 23952-23962.
7. X. Shi, D. Ma, Y. Ma and A. Hu, *J. Photochem. Photobiol. A: Chem.*, 2017, **332**, 487-496.
8. W. J. Chun, A. Ishikawa, H. Fujisawa, T. Takata, J. N. Kondo, M. Hara, M. Kawai, Y. Matsumoto and K. Domen, *J. Phys. Chem. B*, 2003, **107**, 1798-1803.

9. R. Asahi, T. Morikawa, H. Irie and T. Ohwaki, *Chem. Rev.*, 2014, **114**, 9824-9852.
10. N. C. Saha and H. G. Tompkins, *J. Appl. Phys.*, 1992, **72**, 3072-3079.
11. N. D. Shinn and K. L. Tsang, *Journal of Vacuum Science & Technology A: Vacuum, Surfaces, and Films*, 1991, **9**, 1558-1562.
12. J. Lynch, C. Giannini, J. K. Cooper, A. Loiudice, I. D. Sharp and R. Buonsanti, *The Journal of Physical Chemistry C*, 2015, **119**, 7443-7452.
13. J. A. Rodriguez, T. Jirsak, J. Dvorak, S. Sambasivan and D. Fischer, *The Journal of Physical Chemistry B*, 2000, **104**, 319-328.
14. S. Sugai, H. Watanabe, H. Miki, T. Kioka and K. Kawasaki, *Vacuu*, 1990, **41**, 90-92.
15. D. A. Zatsepin, D. W. Boukhvalov, E. Z. Kurmaev, I. S. Zhidkov, N. V. Gavrilov, M. A. Korotin and S. S. Kim, *Appl. Surf. Sci.*, 2015, **355**, 984-988.
16. A. Nambu, J. Graciani, J. A. Rodriguez, Q. Wu, E. Fujita and J. F. Sanz, *J. Chem. Phys.*, 2006, **125**, 094706.
17. S. H. Cheung, P. Nachimuthu, A. G. Joly, M. H. Engelhard, M. K. Bowman and S. A. Chambers, *Surf Sci.*, 2007, **601**, 1754-1762.
18. C. E. Nanayakkara, P. M. Jayaweera, G. Rubasinghege, J. Baltrusaitis and V. H. Grassian, *J. Phys. Chem. A*, 2014, **118**, 158-166.
19. X. Yang, E. Aydin, H. Xu, J. Kang, M. Hedhili, W. Liu, Y. Wan, J. Peng, C. Samundsett, A. Cuevas and S. De Wolf, *Advanced Energy Materials*, 2018, **8**.
20. C. Adelmann, T. Conard, A. Franquet, B. Brijs, F. Munnik, S. Burgess, T. Witters, J. Meersschaut, J. A. Kittl, W. Vandervorst and S. Van Elshocht, *Journal of Vacuum Science & Technology A: Vacuum, Surfaces, and Films*, 2012, **30**.
21. T. Morikawa, S. Saeki, T. Suzuki, T. Kajino and T. Motohiro, *Appl. Phys. Lett.*, 2010, **96**.
22. M. J. Breitschafter, E. Umbach and D. Menzel, *Surf Sci.*, 1981, **109**, 493-511.
23. T. Jirsak, J. Dvorak and J. A. Rodriguez, *Surf Sci.*, 1999, **436**, L683-L690.
24. N. D. Shinn and K. L. Tsang, *Journal of Vacuum Science & Technology A: Vacuum, Surfaces, and Films*, 1990, **8**, 2449-2453.
25. J. A. Rodriguez, T. Jirsak, G. Liu, J. Hrbek, J. Dvorak and A. Maiti, *J. Am. Chem. Soc.*, 2001, **123**, 9597-9605.
26. C. Chen, H. Bai and C. Chang, *The Journal of Physical Chemistry C*, 2007, **111**, 15228-15235.
27. J. A. Rodriguez, T. Jirsak, S. Chaturvedi and J. Dvorak, *J. Mol. Catal. A: Chem.*, 2001, **167**, 47-57.
28. J. H. Thomas and L. H. Hammer, *J. Electrochem. Soc.*, 1989, **136**, 2004-2010.

29. L. A. DeLouise, *Surf Sci.*, 1995, **324**, 233-248.
30. D. Cristea, L. Cunha, C. Gabor, I. Ghiuta, C. Croitoru, A. Marin, L. Velicu, A. Besleaga and B. Vasile, *Nanomaterials (Basel)*, 2019, **9**.
31. S. F. Ho, S. Contarini and J. W. Rabalais, *J. Phys. Chem.*, 1987, **91**, 4779-4788.
32. D. D. Sarma and C. N. R. Rao, *J. Electron. Spectrosc. Relat. Phenom.*, 1980, **20**, 25-45.
33. I. Narkeviciute and T. F. Jaramillo, *Solar RRL*, 2017, **1**.
34. L. Mohan and C. Anandan, *Appl. Surf. Sci.*, 2013, **268**, 288-296.
35. I. Bertoti, M. Mohai, J. L. Sullivan and S. O. Saied, *Appl. Surf. Sci.*, 1995, **84**, 357-371.
36. L. A. de Sena, N. C. C. Rocha, M. C. Andrade and G. A. Soares, *Surface & Coatings Technology*, 2003, **166**, 254-258.
37. B.-H. Lee, Y. D. Kim and K. H. Lee, *Biomaterials*, 2003, **24**, 2257-2266.
38. L. Mohan, C. Anandan and N. Rajendran, *RSC Advances*, 2015, **5**, 41763-41771.
39. J. Guillot, A. Jouaiti, L. Imhoff, B. Domenichini, O. Heintz, S. Zerkout, A. Mosser and S. Bourgeois, *Surf. Interface Anal.*, 2002, **33**, 577-582.
40. G. Lu, S. L. Bernasek and J. Schwartz, *Surf Sci.*, 2000, **458**, 80-90.
41. A. Ganguly, S. Sharma, P. Papakonstantinou and J. Hamilton, *The Journal of Physical Chemistry C*, 2011, **115**, 17009-17019.
42. D. Baurecht and U. P. Fringeli, *Rev. Sci. Instrum.*, 2001, **72**, 3782-3792.
43. G. L. Chiarello and D. Ferri, *Phys. Chem. Chem. Phys.*, 2015, **17**, 10579-10591.
44. D. Ferri, M. A. Newton and M. Nachtegaal, *Top. Catal.*, 2011, **54**, 1070-1078.
45. C. F. J. König, J. A. van Bokhoven, T. J. Schildhauer and M. Nachtegaal, *The Journal of Physical Chemistry C*, 2012, **116**, 19857-19866.